

Accepted Article Preview: Published ahead of advance online publication



## Two-Photon Micro-Printed Ag<sub>2</sub>Te QD–Polymer Hybrid Photonic Platform on Fibre End for Transformative 2D Thermo-Optic Modulation

Zhuojun Wang, Bo Dong, Sengpeng Zhang, Yulong Wang, Ziheng Yu and Changyuan Yu

Cite this article as: Zhuojun Wang, Bo Dong, Sengpeng Zhang, Yulong Wang, Ziheng Yu, Changyuan Yu. Two-Photon Micro-Printed Ag<sub>2</sub>Te QD–Polymer Hybrid Photonic Platform on Fibre End for Transformative 2D Thermo-Optic Modulation. *Light: Advanced Manufacturing* accepted article preview 27 March, 2026; doi: 10.37188/lam.2026.046

This is a PDF file of an unedited peer-reviewed manuscript that has been accepted for publication. LAM are providing this early version of the manuscript as a service to our customers. The manuscript will undergo copyediting, typesetting and a proof review before it is published in its final form. Please note that during the production process errors may be discovered which could affect the content, and all legal disclaimers apply.

Received 3 August 2025; revised 26 March 2026; accepted 26 March 2026;  
Accepted article preview online 27 March 2026

# Two-Photon Micro-Printed Ag<sub>2</sub>Te QD–Polymer Hybrid Photonic Platform on Fibre End for Transformative 2D Thermo-Optic Modulation

Zhuojun Wang<sup>1</sup>, Bo Dong<sup>1, \*</sup>, Sengpeng Zhang<sup>1</sup>, Yulong Wang<sup>1</sup>, Ziheng Yu<sup>1</sup>  
Changyuan Yu<sup>2, \*</sup>

<sup>1</sup> College of Integrated Circuits and Optoelectronic Chips, Shenzhen Technology University, Shenzhen 518118, China

[\\*dongbo@sztu.edu.cn](mailto:*dongbo@sztu.edu.cn)

<sup>2</sup> Hong Kong Polytechnic University, Department of Electrical and Electronic Engineering, Hong Kong, China

[\\*changyuan.yu@polyu.edu.hk](mailto:*changyuan.yu@polyu.edu.hk)

## Abstract

Beyond conventional thermo-optic (TO) devices, this study introduces a groundbreaking hybrid photonic platform incorporating two-photon micro-printed  $\text{Ag}_2\text{Te}$  quantum dots (QDs) within a polymer matrix, which is directly integrated on a fibre end to enable transformative two-dimensional (2D) TO modulation. By leveraging advanced two-photon micro-printing, we precisely fabricated complex hybrid micro-ring resonator (MRR) structures, thereby facilitating unprecedented on-chip integration and intricate three-dimensional geometries that remain unattainable using traditional methods. The proposed platform utilises an  $\text{Ag}_2\text{Te}$  QD-functionalized polymer film, wherein controlled interfacial engineering in conjunction with the intrinsic localised surface plasmon resonance (LSPR) of the QDs amplifies the local optical field by 300% and fundamentally reconfigures photon–thermal–carrier interactions. An innovative 2D synergistic all-optical modulation strategy is employed, leading to substantial performance improvements, including a 19.77-fold enhancement in tuning sensitivity over standard polymer MRRs and 50-fold improvement in modulation speed, reaching up to 100 kHz, which significantly exceeds those of conventional TO platforms. This compact fibre-integrated architecture, enabled by precision additive manufacturing, delivers a robust, energy-efficient, and high-speed solution for dynamically reconfigurable on-chip TO modulation and represents a transformative step forward for integrated photonic circuits.

**Keywords:** Micro-ring resonator, Quantum dot, Thermo-optic effect, All-optical control

## Introduction

Reconfigurable photonic integrated circuits (PICs)<sup>1-5</sup> are at the forefront of next-generation optical information processing, offering dynamic control over light propagation, filtering,<sup>6, 7</sup> and switching within chip-scale platforms.<sup>8, 9</sup> Among the various modulation schemes, thermo-optic (TO) tuning<sup>10-14</sup> has garnered significant attention owing to its broadband compatibility, low insertion loss, and ease of integration with complementary metal-oxide-semiconductor (CMOS) processes. In particular, micro-ring resonators (MRRs), characterised by their compact footprint and high-quality factor,<sup>15</sup> serve as fundamental building blocks for TO modulators, enabling applications in optical communications,<sup>16</sup> wavelength division multiplexing,<sup>17</sup> sensing,<sup>18</sup> and signal processing.<sup>19</sup>

Polymer MRRs have been widely explored for TO tuning because of their straightforward fabrication,<sup>20</sup> large TO coefficients,<sup>21, 22</sup> and mechanical flexibility.<sup>23</sup> However, their performance is fundamentally constrained by the slow thermal response associated with the large heat capacity and low thermal conductivity of polymer waveguide materials, as well as inefficient heat dissipation mechanisms. Consequently, conventional polymer TO modulators typically exhibit sub-kHz switching speeds,<sup>24</sup> low tuning efficiency,<sup>25</sup> and significant performance drift under ambient temperature fluctuation,<sup>26</sup> which hinder their deployment in high-speed or thermally dynamic environments.

To address these bottlenecks, numerous studies have explored enhancing photothermal modulation via the integration of functional nanomaterials and geometric optimisation of photonic devices. Incorporating low-dimensional materials or metallic nanostructures has led to improvements in TO sensitivity and switching dynamics.<sup>27-29</sup>

Nevertheless, these strategies predominantly operate within a one-dimensional (1D) thermal modulation framework, in which optical excitation is applied either laterally along the waveguide or vertically across the substrate. Such geometrically constrained heating paths limit the spatiotemporal control of the thermal field, often resulting in inefficient energy utilisation and a suboptimal modulation response. In addition to material constraints, the inherently planar design of conventional on-chip architectures further limits the spatial degrees of freedom for photothermal excitation. By contrast, fibre-integrated microcavity platforms provide superior optical confinement and more localised pump delivery by leveraging the dimensional flexibility of the fibre end-face coupling. This configuration enables both on-chip pumping and efficient pump delivery via fibre, providing a thermally favourable setup for enhanced photothermal modulation.

Furthermore, functional coatings employed in prior studies predominantly lack the nanoscale structural precision and uniform optical–thermal coupling required for highly localised, fast, and efficient modulation. The thermal diffusion volumes and interfacial coupling remain insufficiently controlled at the subwavelength scale, which hinders further enhancements in speed, power consumption, and integration flexibility. These limitations highlight the need for alternative material platforms that are capable of enabling multidimensional and finely tuneable photothermal interactions within on-chip photonic architectures.

Quantum dots (QDs) have recently gained traction as a versatile class of nanomaterials for photonic integration, offering strong broadband light absorption, size-tuneable optoelectronic properties, and solution-processable compatibility with diverse substrates.<sup>30</sup> Their unique optoelectronic characteristics have enabled significant advances in integrated quantum photonic circuits,<sup>31</sup> metasurface and cavity-based light–matter interaction platforms,<sup>32</sup> and chip-scale light emitters and optoelectronic devices.<sup>33</sup> Beyond established roles in photonic emission and absorption

processes, QDs also exhibit highly efficient photothermal conversion that rapidly transforms optical excitation into localized heat.<sup>34-37</sup> This nanoscale heat generation, amplified by the strong absorption cross-section and fast non-radiative relaxation of QDs, provides an effective mechanism for driving refractive-index modulation in adjacent polymer waveguides through their TO coefficient. As such, QDs offer strong yet underexplored potential for enabling active photothermal tuning in reconfigurable polymer photonic platforms.

The present study introduces a novel on-chip MRR system, precisely fabricated via advanced two-photon micro-printing, which fundamentally moves beyond conventional limitations by leveraging an Ag<sub>2</sub>Te QD film for transformative two-dimensional (2D) TO modulation. This cutting-edge three-dimensional (3D) additive manufacturing technique is pivotal because it enables direct, high-resolution fabrication of intricate MRR geometries and their seamless integration onto the fibre end, which is unachievable using traditional planar lithography. Through meticulous QD–polymer interfacial engineering, the Ag<sub>2</sub>Te QD film is precisely integrated within a pentaerythritol tetraacrylate (PETA)-based MRR structure, forming a truly hybrid photonic platform whose complex architecture is uniquely enabled by two-photon micro-printing. Crucially, we introduce an innovative 2D all-optical modulation strategy that employs one pump beam propagating along the MRR waveguide and a second beam perpendicular to the structure via the substrate. This synergistic approach, combined with the Ag<sub>2</sub>Te QD layer's intrinsic localized surface plasmon resonance (LSPR) that enhances local optical field intensity by an excellent 300%, yields unprecedented performance. Experimental results demonstrate a remarkable 19.77-fold enhancement in tuning sensitivity (reaching  $-104 \text{ pm mW}^{-1}$ ) compared with the uncoated polymer MRR in conjunction with a 50-fold improvement in modulation speed that extends the dynamic response to 100 kHz. This response significantly exceeds the kHz-level performance of representative polymer TO modulators reported in the literature.<sup>38</sup> Furthermore, QD integration facilitated by the precision of two-

photon micro-printing significantly improves the quality factor (Q-factor), extinction ratio, and mode confinement while reducing scattering via optimised interfacial phonon modulation. This study significantly expands the functional scope of QDs in integrated polymer photonics and pioneers a multidimensional, high-speed, and energy-efficient modulation strategy critical for future reconfigurable optical systems.

## Fabrication and characterization

### Two-photon micro-printed platform on fibre end

**Fig.1a** illustrates the fabrication process for directly constructing polymer MRRs on optical fibre facets. The fibre cladding was first carefully stripped, and the facet was cleaned using anhydrous ethanol to ensure a smooth surface and strong adhesion of the photoresist. The prepared fibre was then vertically inserted into a droplet of PETA<sup>39</sup> resin deposited on a glass substrate, followed by inverted laser writing.

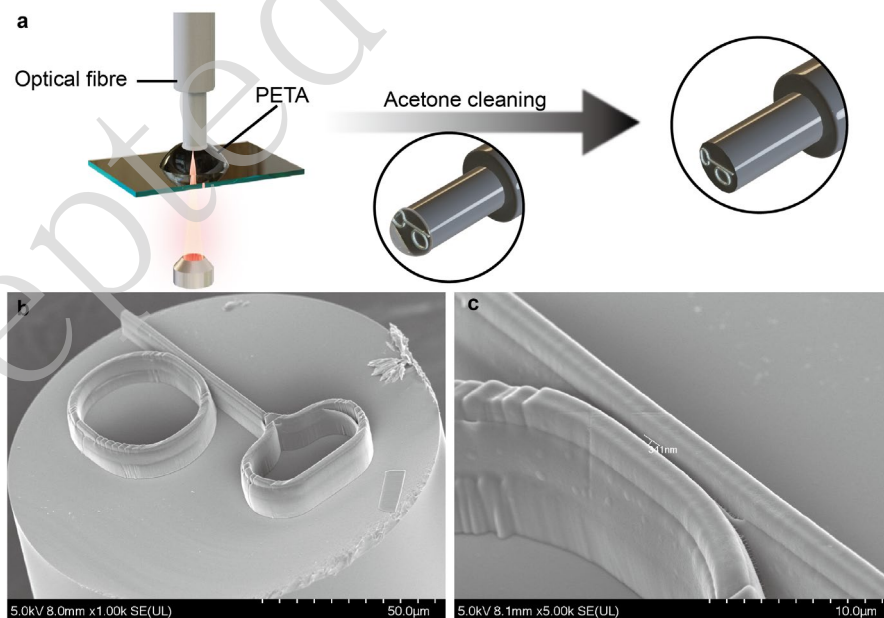


**Fig. 1** **a** TPP printing of a PETA micro-ring on a fibre end. **b** SEM image of the printed MRR. **c** Zoomed-in view showing a 341 nm coupling gap.

The structure was fabricated via two-photon polymerisation (TPP),<sup>40, 41</sup> enabling submicron resolution. Under tightly focused femtosecond pulses, polymerisation occurred only at the focal point where two-photon absorption is simultaneously satisfied, confining the solidification to a nanoscale voxel. Precise 3D scanning of the focal spot across the fibre core region enabled direct writing of high-fidelity micro-ring structures onto the facet with excellent spatial accuracy.

After printing, the fibre facet was immersed in acetone for approximately 1 min to remove uncured resin, leaving only the fully polymerised resonator. **Fig. 1b** presents an SEM image of the fabricated MRR, showing smooth surfaces and well-defined boundaries. A magnified view of the coupling region (**Fig. 1c**) reveals a gap of 341 nm, which closely aligns with the designed 300 nm, thereby confirming the high precision and structural fidelity achievable with TPP on fibre-based platforms. The finite-difference time-domain (FDTD) simulations reported in the Supplementary Information (**Fig. S1**) further indicate that this small deviation exerts a negligible impact on the resonance characteristics.

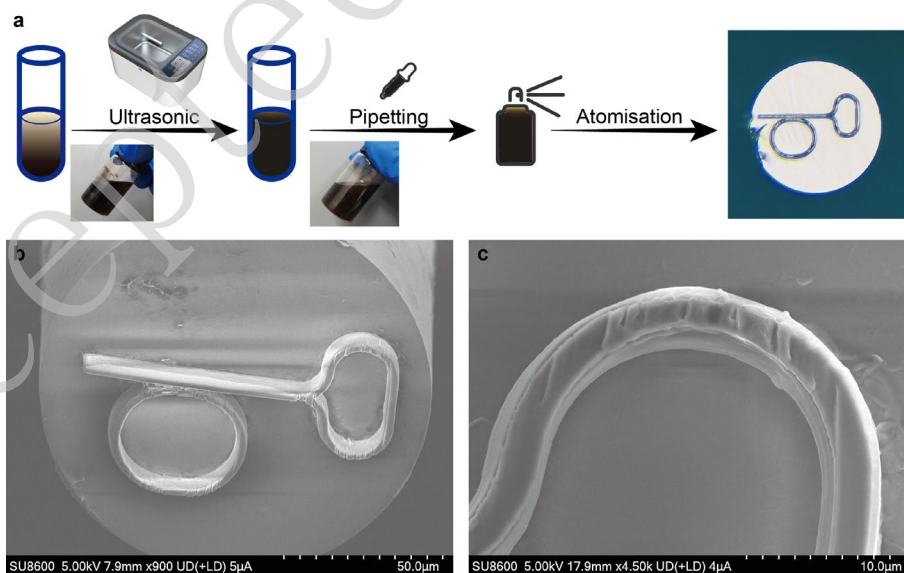


**Fig. 2** a Fabrication of  $\text{Ag}_2\text{Te}$  QD film via spray-coating. b SEM image of the QD-coated MRR surface. c Zoomed-in view of the QD-coated surface.

**Fig. 2a** outlines the key fabrication steps involved in integrating  $\text{Ag}_2\text{Te}$  QDs onto the entire MRR structure via a controlled spray-coating process. Following the controlled spray-coating of  $\text{Ag}_2\text{Te}$  QDs onto the MRR surface, comprehensive structural and optical characterisations were performed to assess the quality and uniformity of the QD layer. The SEM image in **Fig. 2b** confirms successful attachment of the QDs to the device surface, effectively filling small cracks and grooves, which enhanced the surface smoothness. The magnified view in **Fig. 2c** further illustrates this effect, demonstrating how the QD coating smooths surface irregularities, thereby improving uniformity. Additional atomic force microscopy (AFM) measurements of the QD-coated surface revealed a root-mean-square roughness ( $R_a$ ) of approximately 0.652 nm, further demonstrating the smoothness and uniformity of the QD layer. An AFM image of the QD-coated surface is provided in the Supplementary Information (**Fig. S2**). These observations indicate that the spray-coating process successfully provides uniform coverage, which is crucial for the enhanced optical modulation performance of the device.

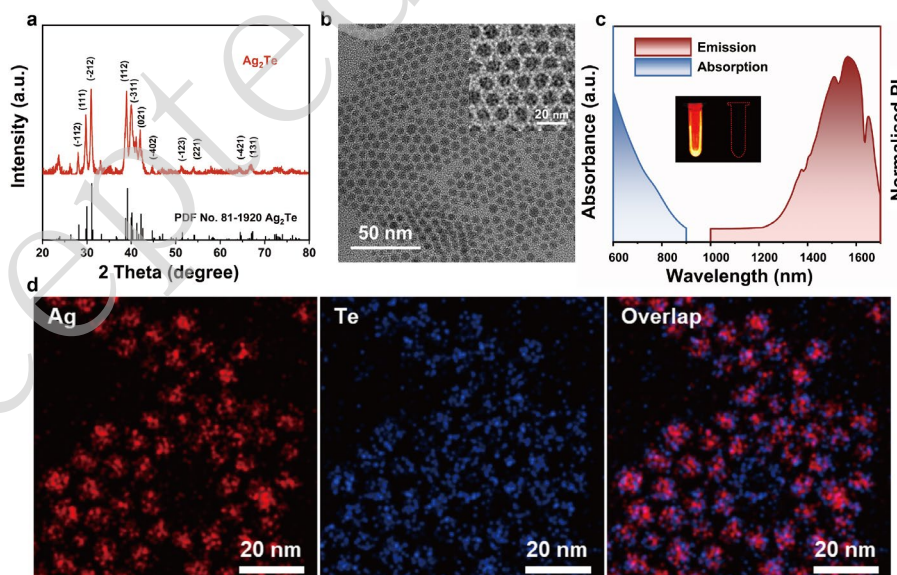


**Fig. 3** **a** XRD pattern. **b** TEM image with lattice fringes. **c** Absorption and PL spectra. **d** EDS elemental mapping of Ag and Te.

As shown in **Fig. 3a**, the X-ray diffraction (XRD) pattern of the Ag<sub>2</sub>Te QDs closely aligns with the standard cubic phase of Ag<sub>2</sub>Te (PDF No. 81-1920), with no detectable impurity peaks, confirming the high phase purity and crystalline quality of the synthesised QDs. This structural integrity ensures consistent optical absorption and thermal properties throughout the QD film.

Transmission electron microscopy (TEM) analysis (**Fig. 3b**) revealed that the Ag<sub>2</sub>Te QDs are uniformly dispersed without prominent aggregation, exhibiting a narrow size distribution with an average diameter of  $5.1 \pm 0.7$  nm. The good morphological uniformity of the QDs is beneficial for achieving relatively uniform surface coverage when deposited onto the curved MRR structure via spray-coating. The corresponding particle size distribution histogram is provided in the Supporting Information (**Fig. S3**).

The optical properties of the QDs were assessed by UV-VIS-NIR absorption and photoluminescence (PL) spectroscopy (**Fig. 3c**). The absorption profile spans the visible to near-infrared range and exhibits PL emission peaks at 1560 nm. This NIR-II emission overlaps favourably with the operating wavelength of the MRR (1550 nm), supporting efficient pump–probe energy transfer. For NIR-II fluorescence imaging, the Ag<sub>2</sub>Te QDs were excited using an 808 nm laser, as illustrated by the bright luminescence shown in the inset, highlighting their strong optical activity and suitability for photothermal conversion.

To further confirm the chemical composition and elemental uniformity of the synthesised Ag<sub>2</sub>Te QDs prior to integration, energy-dispersive X-ray spectroscopy (EDS) mapping was conducted on a drop-cast Ag<sub>2</sub>Te QD film (**Fig. 3d**). The elemental maps of Ag and Te exhibit strong co-localisation and homogeneous spatial distribution across the sample. These results confirm the chemical homogeneity and nanoscale compositional uniformity of the QDs, which are essential for achieving consistent photothermal performance when incorporated into photonic devices.

Collectively, these structural and optical characterisations confirmed the successful synthesis and uniform deposition of high-quality  $\text{Ag}_2\text{Te}$  QDs on the MRR surface. The crystalline structure, broadband NIR-II response, and uniform distribution of the material collectively provide a robust foundation for efficient and reproducible TO modulation in hybrid QD–polymer photonic devices.

## Results and discussion

### Enhanced static optical performance and depth coherence modulation in QD-coated MRR

The integration of the  $\text{Ag}_2\text{Te}$  QD film yielded a substantial improvement in the static optical characteristics of the MRR, which was attributed to the combined effects of refractive index modulation, near-field confinement, and scattering suppression. **Fig. 4a** presents a schematic of the QD-coated MRR, where the entire PETA-based waveguide structure is uniformly coated with  $\text{Ag}_2\text{Te}$  QDs. In addition to spectral measurements, FDTD simulations were performed to visualise the influence of  $\text{Ag}_2\text{Te}$  QDs on local field enhancement. As illustrated in **Fig. 4b**, the spatial distribution of the normalised electric field intensity ratio,  $|E_{\text{coated}}|^2/|E_{\text{bare}}|^2$ , revealed a pronounced localised enhancement in the region corresponding to the main micro-ring waveguide. In particular, the field intensity ratio reached a peak value of approximately 3 at the waveguide–QD interface while remaining close to unity in most other regions of the cavity. The enhancement was mainly concentrated in the vicinity of the waveguide–QD interface, indicating strong near-field confinement and elevated energy density. This field enhancement is partly attributed to the plasmon-assisted effects from the  $\text{Ag}_2\text{Te}$  QDs, which exhibit mild LSPR behaviour under optical excitation. These effects, in combination with surface smoothing and refractive modulation, enhance the optical circulation efficiency within the cavity.

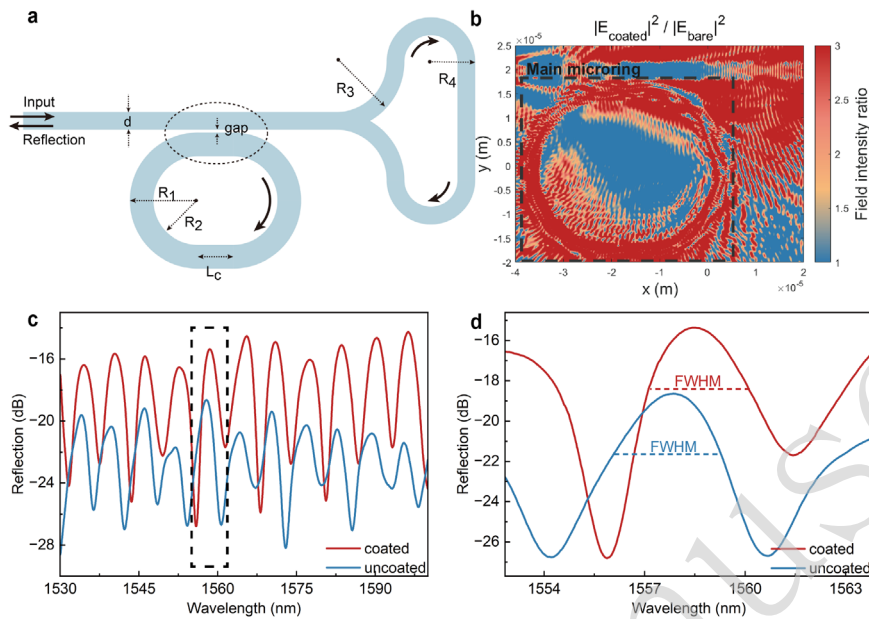


**Fig. 4** **a** Schematic of the MRR. **b** FDTD simulation showing the spatial distribution of electric field intensity enhancement factor ( $|E_{\text{coated}}|^2 / |E_{\text{bare}}|^2$ ), with the main micro-ring region highlighted. **c** Reflection spectra before and after QD integration, revealing increased resonance depth. **d** FWHM comparison at  $\lambda_0 \approx 1558$  nm, indicating improved quality factor after coating.

As shown in **Fig. 4c**, the broadband reflection spectrum reveals a substantial increase in the reflection depth across multiple resonance dips following QD integration. At 1558 nm, the resonance depth improved from 7.92 dB to 11.41 dB, indicating higher contrast and enhanced optical feedback efficiency. This enhancement originates from the QD-induced refractive index modulation and resulting modification of the guided mode boundary conditions. The high refractive index and nanoscale dimensions of the  $\text{Ag}_2\text{Te}$  QDs alter the modal distribution and optical confinement at the waveguide surface, thereby influencing the balance between intrinsic cavity loss and external coupling. Simulated fundamental mode profiles before and after QD coating at 1558 nm are provided in the Supplementary Information (**Fig. S4**), confirming the QD-induced redistribution of the guided mode. In addition, the conformal QD layer can suppress surface-related scattering losses, jointly contributing to the observed improvement in the resonance contrast.

In addition to the improvement in reflection amplitude, a marginal redshift of the resonance wavelength was observed, which is attributed to an increased effective refractive index  $n_{\text{eff}}$  owing to the high polarisability of the QD layer. The resonance condition is expressed as

$$\lambda = \frac{n_{\text{eff}}L}{m} \quad (1)$$

where  $\lambda$  denotes the resonance wavelength,  $L$  is the cavity length, and  $m$  represents the resonance mode number. According to this condition, the observed spectral shift confirms perturbative modification of the optical path length via surface coating.

Furthermore, the Q-factor is defined as the ratio of the stored optical energy to the energy dissipated per cycle and serves as a critical parameter for assessing MRR performance. It is quantitatively expressed as follows

$$Q = \frac{\lambda}{\Delta\lambda_{\text{FWHM}}} \quad (2)$$

where  $\Delta\lambda_{\text{FWHM}}$  represents the full width at half-maximum (FWHM) of the resonance in the reflection spectrum. As shown in **Fig. 4d**, at  $\lambda \approx 1558 \text{ nm}$  under zero-pump conditions, the application of the QD film narrows the resonance width from 3.24 nm to 2.94 nm, increasing the Q-factor from 480.86 to 530.09, corresponding to an approximate 10.24% enhancement. This change reflects a modest reduction in the effective optical loss associated with QD-induced modification of the modal boundary conditions.

Collectively, these improvements underscore the pivotal role of plasmonic QD films in strengthening light–matter interactions, minimising optical losses, and enabling high-coherence operation within compact photonic architectures. This synergistic effect highlights the potential of QD-based nanocomposites as versatile building blocks for reconfigurable, high-performance on-chip photonic systems.

Building upon these static performance gains, the following sections demonstrate that QD integration also significantly enhances the TO tuning sensitivity under optical pumping, enabling more efficient dynamic modulation under reduced excitation power.

## 2D all-optical modulation of Ag<sub>2</sub>Te-coated MRR

This study systematically investigated the pump-probe modulation response of a QD-coated MRR under 2D optical control using an integrated micro-ring photonic circuit. The experimental architecture is illustrated in **Fig. 5a**. A broadband source (BBS, 1525–1600 nm) was employed as the primary probe light, whereas a 980-nm continuous-wave laser served as the excitation pump. The BBS was launched into Port 1 of an optical circulator (OC) and combined with the first 980-nm pump branch via a 1×2 fibre coupler. The collimated beam was then edge-coupled into the MRR using a 60° fibre lens, aligned parallel to the in-plane waveguide. The reflected signal exited through Port 2 of the OC and was analysed using an optical spectrum analyser (OSA).

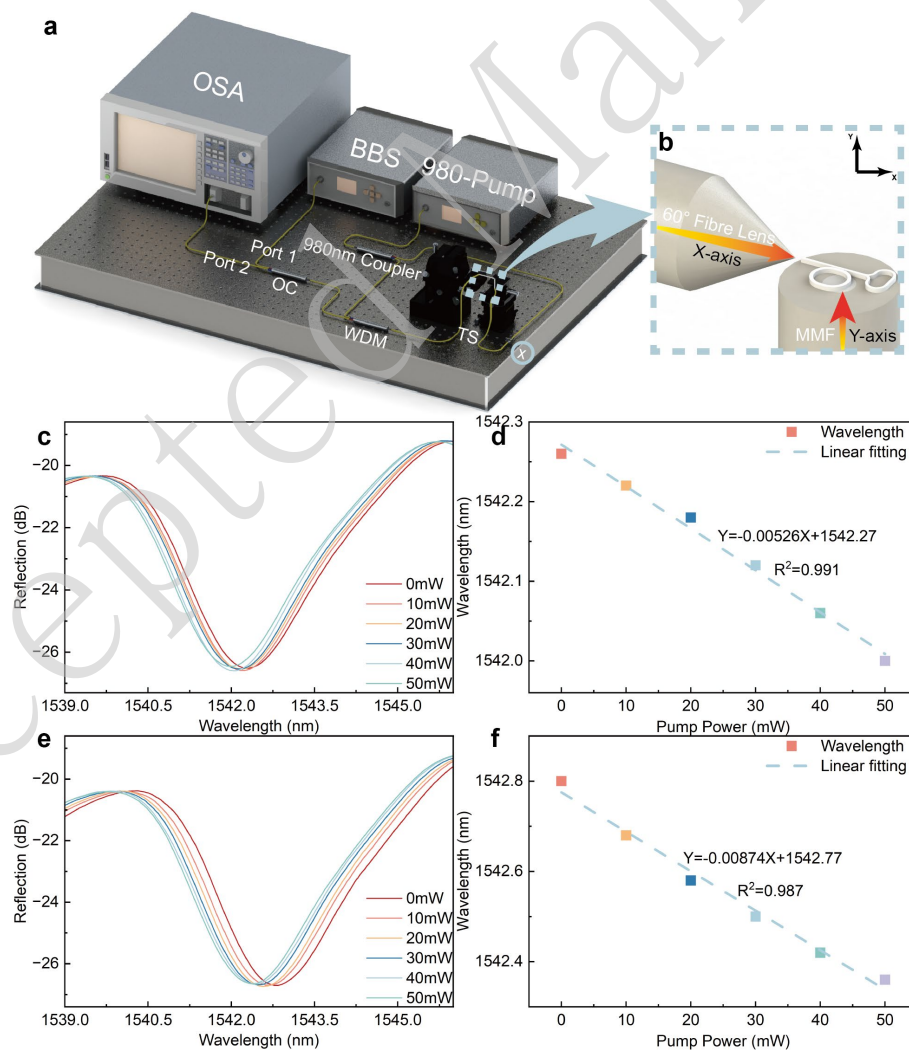


**Fig. 5 a** Schematic of the optical measurement setup. **b** Enlarged view showing the 2D pumping configuration with one pump light along the MRR waveguide and the other perpendicular to the MRR waveguide via the substrate. **c,d** Reflection spectra and linear fitting of resonance shift under x-axis (1D) pumping for the uncoated MRR (without QDs). **e,f** Reflection spectra and linear fitting under combined x- and y-axis (2D) pumping for the uncoated MRR (without QDs).

For clarity, the direction along the MRR waveguide, which is parallel to the fibre end surface, is defined as the x-axis. The axis perpendicular to the MRR waveguide, i.e., normal to the fibre end surface, is designated as the y-axis. 1D modulation refers to optical pumping applied individually along either the x- or y-axis, whereas 2D modulation involves simultaneous excitation along both directions.

To enable 2D all-optical modulation, a second pump beam branch was delivered perpendicularly through the substrate via a multimode fibre (MMF). As illustrated in **Fig. 5b**, the system supports switching between 1D and 2D modulation modes by selectively disconnecting the optical path at position X. The 60° fibre lens was mounted on a precision translation stage to ensure accurate alignment with the x-axis excitation path. This dual-axis pumping strategy utilises spatially separated optical channels, enabling the decoupled and efficient control of the photonic device along orthogonal axes. Furthermore, the system is inherently compatible with wavelength-division-multiplexing (WDM)-free operation.

Baseline measurements were conducted employing uncoated PETA-based MRR under both 1D and 2D pumping schemes. As shown in **Fig. 5c**, increasing the 980-nm pump power from 0 to 50 mW under x-axis-only pumping (1D) resulted in a resonance blueshift of 0.2 nm, corresponding to a tuning sensitivity of  $-5.26 \text{ pm mW}^{-1}$ , with a linearity of  $R^2 = 0.951$  (**Fig. 5d**). Under combined x- and y-axis (2D) pumping for the uncoated MRR (**Fig. 5e**), the resonance shifts marginally increased to 0.42 nm, with a linearity of  $R^2 = 0.987$  (**Fig. 5f**), corresponding to an improved tuning sensitivity of  $-8.74 \text{ pm mW}^{-1}$ .

The observed resonance shifts in the uncoated MRR originate primarily from the intrinsic TO effect of the polymeric waveguide. As PETA exhibits a negative TO coefficient ( $dn/dT < 0$ ), its refractive index decreases with increasing temperature. This temperature-induced reduction in  $n_{\text{eff}}$  shortens the optical path length of the cavity, producing a blueshift in the resonance wavelength under optical pumping. The resonance condition is governed by **Equation 1**, and the subsequent analysis quantifies the temperature-dependent variations in refractive index and effective cavity length. Under 980-nm continuous-wave excitation, weak absorption in the PETA waveguide leads to localised heating. The volumetric heat power density can be expressed as

$$Q_{\text{gen}} = \alpha_{\text{WG}} \cdot I_{\text{pump}} = \alpha_{\text{WG}} \cdot \left( \frac{P_{\parallel}}{A_{\parallel}} + \frac{P_{\perp}}{A_{\perp}} \right) \quad (3)$$

where  $I_{\text{pump}}$  is the total pump intensity and  $\alpha_{\text{WG}}$  is the absorption coefficient of the PETA.  $P_{\parallel}$  and  $P_{\perp}$  are the pump power in the x- and y-axes, respectively, and  $A_{\parallel}$  and  $A_{\perp}$  represent the corresponding optical mode areas.

The resulting increase in temperature induces both a refractive index variation via the TO effect and physical expansion of the polymeric waveguide. A detailed derivation of the steady-state heat conduction, average increase in temperature, and associated TO-induced refractive index modulation is provided in the Supplementary Information (S5–S7).

By jointly considering the TO-induced refractive index change and thermally induced expansion of the micro-ring cavity, the total resonant wavelength shift can be expressed as

$$\Delta\lambda = \lambda \cdot \left( \frac{\Gamma}{n_{\text{eff}}} \cdot \frac{dn_{\text{eff}}}{dT} + \alpha_{\text{eff}} \right) \cdot \left( \frac{\alpha_{\text{WG}} \cdot V}{h_{\text{eff}}} \right) \cdot \left( \frac{P_{\parallel}}{A_{\parallel}} + \frac{P_{\perp}}{A_{\perp}} \right) \quad (4)$$

where  $\Gamma$  is the overlap factor between the guided optical mode and thermally perturbed region,  $n_{\text{eff}}$  is the effective refractive index of the guided mode,  $\alpha_{\text{eff}}$  denotes the effective thermal expansion coefficient of the polymer waveguide,  $V$  represents the effective heated volume, and  $h_{\text{eff}}$  is the equivalent heat dissipation coefficient. For the

uncoated MRR, the relatively small absorption coefficient  $\alpha_{\text{WG}}$  and large heat dissipation coefficient  $h_{\text{eff}}$  limit the achievable modulation efficiency. Although 2D pumping increases the effective heating volume  $V$ , the overall enhancement in tuning efficiency remains modest owing to the intrinsic material limitations of the polymer waveguide.

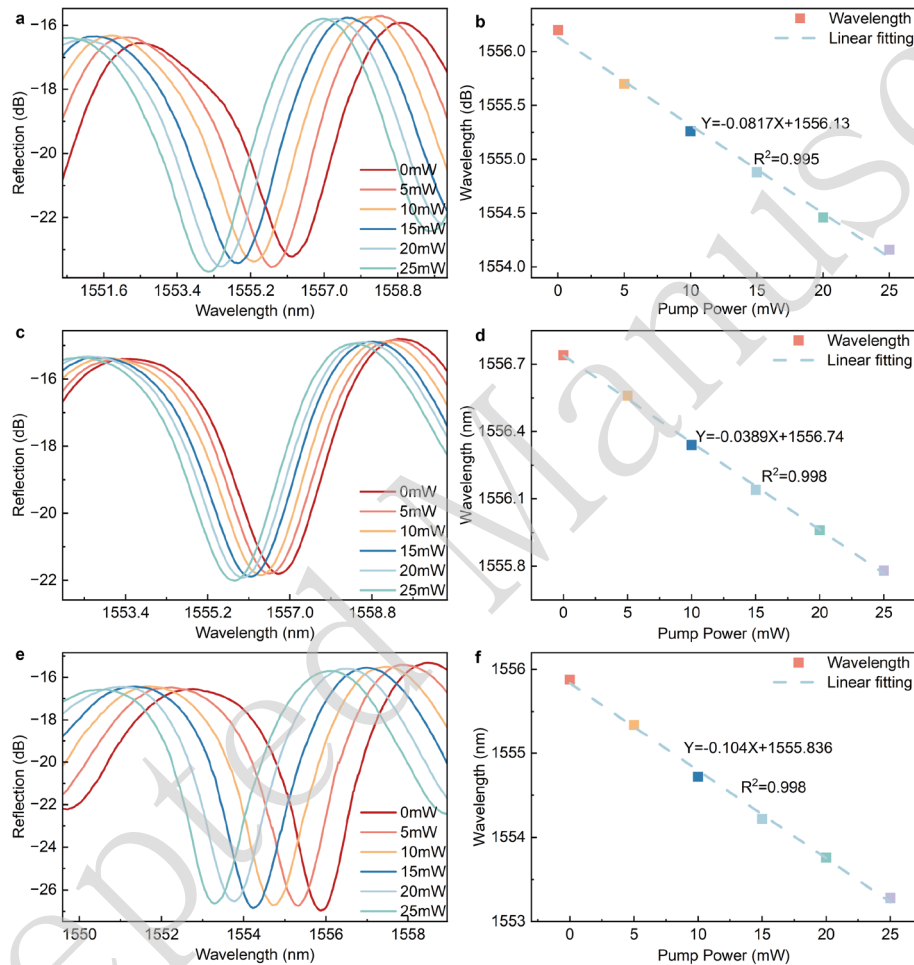


**Fig. 6** a,b Reflection spectra and linear fitting of resonance shift under x-axis excitation. c,d Corresponding spectral evolution and linear regression under y-axis pumping. e,f Enhanced resonance shift and linearity achieved under combined x- and y-axis (2D) optical pumping.

Upon integration of the  $\text{Ag}_2\text{Te}$  QD film, the MRR exhibited a significantly enhanced photothermal tuning response owing to improved light absorption and heat conversion efficiency. Notably, although the QD layer significantly enhanced the optical absorption and local heating, the guided optical mode remained primarily

confined within the PETA core. Because PETA exhibits a negative TO coefficient, the temperature-induced reduction in the core refractive index continues to dominate the effective index variation of the hybrid waveguide. Consequently, the resonance wavelength still exhibits a blueshift under pump illumination after QD coating. As shown in **Fig. 6a**, under 1D modulation with optical pumping along the x-axis, the resonance wavelength blueshifts by 2.04 nm, corresponding to a tuning sensitivity of  $-81.7 \text{ pm mW}^{-1}$ . This response exhibits a high degree of linearity with a correlation coefficient of  $R^2 = 0.995$  (**Fig. 6b**). This value represents a 15.53-fold improvement in sensitivity compared with that of the uncoated device.

When the pump light is applied along the y-axis, the resonant wavelength shifts by 0.96 nm (**Fig. 6c**), resulting in a tuning sensitivity of  $-38.9 \text{ pm mW}^{-1}$  and excellent linearity ( $R^2 = 0.998$ , **Fig. 6d**). Under 2D modulation—simultaneous excitation along both the x- and y-axes—the resonance shift increases further to 2.60 nm (**Fig. 6e**), corresponding to an improved tuning sensitivity of  $-104 \text{ pm mW}^{-1}$  with sustained linearity ( $R^2 = 0.998$ , **Fig. 6f**).

This significant improvement results from the synergistic enhancement of light–matter interaction and photothermal conversion within the  $\text{Ag}_2\text{Te}$  QD layer. Photothermal conversion enabled by rapid non-radiative relaxation constitutes the dominant mechanism for TO modulation, whereas enhanced light–matter interaction primarily increases the effective optical absorption. The QD film exhibits efficient photon absorption via interband transitions and LSPR, which enhances the local optical field and increases the absorption cross-section. The effective absorption cross-section is expressed as

$$\sigma_{\text{eff}}(\omega_p) = \sigma_{\text{QD}} \cdot G_{\text{plasmon}} \quad (5)$$

where  $\sigma_{\text{QD}}$  is the intrinsic absorption cross-section of the QDs, and  $G_{\text{plasmon}} = \left| \frac{E_{\text{local}}(\omega_p)}{E_0(\omega_p)} \right|^2$  represents the field enhancement factor attributed to plasmonic resonance, where  $E_{\text{local}}(\omega_p)$  and  $E_0(\omega_p)$  are the localised and incident electric field intensities,

respectively. This mechanism amplifies absorption by a factor of  $G_{\text{plasmon}}$ . Rapid non-radiative carrier relaxation (lifetime  $\tau_{\text{NR}}$ ) results in localised heat generation

$$P_{\text{heat,QD}} = \eta_{\text{NR}} \cdot \eta_{\text{mig}} \cdot (\hbar\omega_p / \tau_{\text{NR}}) \quad (6)$$

where  $\eta_{\text{NR}} \approx 1$  denotes the non-radiative efficiency,  $\eta_{\text{mig}}$  is the thermal migration efficiency, and  $\hbar\omega_p$  is the excitation photon energy. The resulting volumetric heat power density is expressed as

$$Q_{\text{gen}} = N_{\text{QD}} \cdot \sigma_{\text{eff}} \cdot \left( \frac{P_{\parallel}}{A_{\parallel}} + \frac{P_{\perp}}{A_{\perp}} \right) \cdot \eta_{\text{eff}} \quad (7)$$

where  $N_{\text{QD}}$  is the QD areal density, and  $\eta_{\text{eff}} = \eta_{\text{NR}} \cdot \eta_{\text{mig}}$  denotes the total energy conversion efficiency. Consequently, the resonant wavelength shift  $\Delta\lambda_{\text{QD}}$  can be expressed as

$$\Delta\lambda_{\text{QD}} = \lambda_{\text{QD}} \cdot \left( \frac{\Gamma}{n'_{\text{eff}}} \cdot \frac{dn'_{\text{eff}}}{dT} + \alpha'_{\text{eff}} \right) \cdot \frac{N_{\text{QD}} \cdot \sigma_{\text{QD}} \cdot G_{\text{plasmon}} \cdot \eta_{\text{eff}} \cdot V}{h_{\text{eff}}} \left( \frac{P_{\parallel}}{A_{\parallel}} + \frac{P_{\perp}}{A_{\perp}} \right) \quad (8)$$

where  $\lambda_{\text{QD}}$  is the resonance wavelength of the MRR after being coated with  $\text{Ag}_2\text{Te}$  QDs, and  $\alpha'_{\text{eff}}$  represents the effective thermal expansion coefficient of the  $\text{Ag}_2\text{Te}$  QD-coated structure, which incorporates the modified thermo-mechanical response of the hybrid waveguide. This model predicts that the 2D modulation response should approximate the sum of shifts obtained under individual x- and y-axis pumping. However, the experimental results exhibit a marginal but consistent sublinear response, indicating that interaction-related thermal effects, such as the partial overlap of temperature fields under dual-axis excitation, become non-negligible.

To incorporate this deviation from the ideal additive behaviour, the model is refined by introducing a thermal interaction correction factor,  $\eta_{\text{overlap}}$ , which captures the reduction in effective temperature rise resulting from partial overlap of the thermal diffusion regions generated by the two pump beams

$$\Delta\lambda_{\text{res}}^{2\text{D}} = \eta_{\text{overlap}} (\Delta\lambda_{\text{res}}^{\parallel} + \Delta\lambda_{\text{res}}^{\perp}) \quad (9)$$

where  $\eta_{\text{overlap}} < 1$  represents the degree of thermal redundancy when both pump-induced heat sources share common dissipation pathways within the polymer waveguide and substrate.

In addition to thermal field overlap, secondary effects, such as nonlinearity in the TO coefficient at elevated temperatures and partial saturation of QD absorption, may further suppress the ideal additive response. To quantitatively evaluate the dominant contribution from thermal overlap,  $\eta_{\text{overlap}}$  was extracted employing a linear least-squares regression, where the experimentally measured 2D resonance shifts were fitted against the theoretical additive prediction  $\Delta\lambda_{\parallel} + \Delta\lambda_{\perp}$  over the full pump-power range shown in **Fig. 6**.

The fitting yielded  $\eta_{\text{overlap}} \approx 0.87$ , indicating that approximately 13% of the theoretical additive shift was suppressed under realistic 2D excitation conditions. This experimentally-derived correction factor provides a compact and physically motivated description of the interaction-induced deviation without introducing additional free parameters and highlights the importance of thermal coupling effects in 2D photothermal modulation.

Collectively, the experimental and theoretical results demonstrate that the enhanced tuning sensitivity stems from optimised photon-QD interactions enabled by spectral matching, local field amplification, and efficient heat generation, all facilitated by the  $\text{Ag}_2\text{Te}$  QD film. Further enhancement can be achieved by engineering higher QD densities, more efficient plasmonic structures (to increase  $G_{\text{plasmon}}$ ), or reducing the thermal resistance (lower  $h_{\text{eff}}$ ). These findings provide a comprehensive design framework for developing high-sensitivity, dynamically-tuneable photonic devices and underscore the potential of functional QD–polymer hybrid materials in reconfigurable integrated optoelectronics.

### **Dynamic all-optical modulation of $\text{Ag}_2\text{Te}$ QD-coated MRR**

To investigate the dynamic modulation behaviour of  $\text{Ag}_2\text{Te}$  QD film-coated MRR, a single-wavelength laser with an output wavelength of 1552.22 nm was used as the probe signal. As illustrated in **Fig. 7**, the dynamic modulation system comprised a computer-controlled signal generator that drives an acoustic-optic modulator (AOM) to modulate a 980-nm pump laser, producing a square-wave optical excitation. The modulated pump light is routed through a fibre coupler and can be selectively delivered either along the MRR waveguide via a WDM for 1D modulation or simultaneously through an additional branch perpendicular to the substrate via an MMF for 2D modulation. The switching between 1D and 2D dynamic modulation is realised by connecting or disconnecting the secondary pump branch at position X, as indicated in **Fig. 7**, ensuring that both modulation schemes are implemented within the same optical architecture. The 1550 nm signal light is launched into the MRR via an OC and WDM. The reflected signal is measured in real-time using a high-speed oscilloscope after being detected using a photodetector (PD).

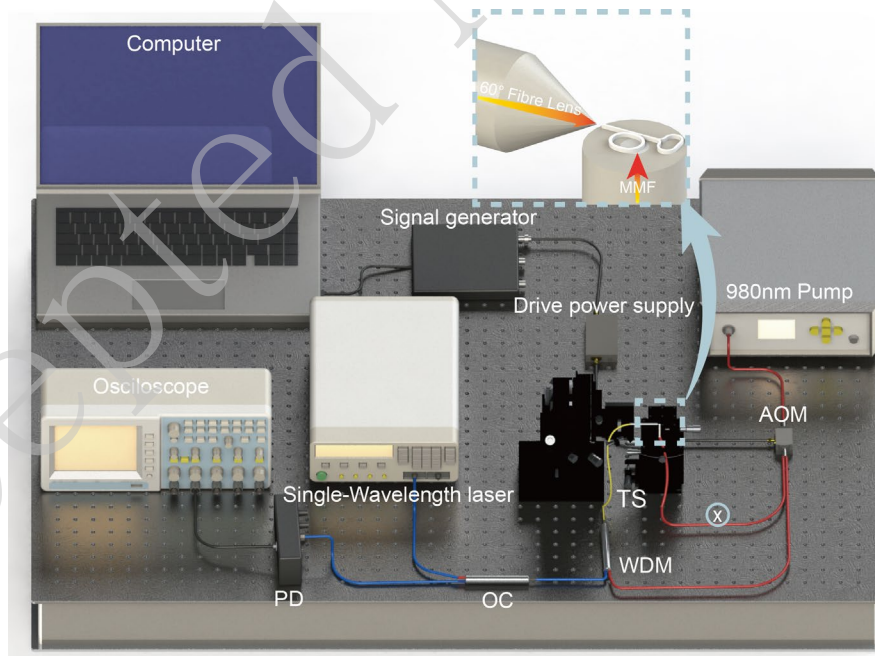


**Fig. 7** Dynamic modulation system for switchable 1D and 2D modulation.

The dynamic modulation mechanism extends the static TO tuning model by introducing a time-varying pump power

$$P_{\text{pump}}(t) = \Delta P_0 + \Delta P \cdot \text{square}(2\pi ft) \quad (10)$$

where  $f$  denotes the modulation frequency. Based on the resonant shift model given in **Equation 8**, the temporal evolution of the resonant wavelength can be expressed as

$$\Delta\lambda(t) = \Delta\lambda \cdot \text{square}(2\pi ft + \phi) \quad (11)$$

where the peak shift  $\Delta\lambda$  is determined by static parameters, including  $N_{\text{QD}}$ ,  $\sigma_{\text{eff}}$ , and  $h_{\text{eff}}$ . The phase delay  $\phi$ , which is governed by thermal inertia, is given by  $\phi = \arctan(f/f_c)$ ,  $f_c = 1/(2\pi\tau_{\text{thermal}})$ . This dynamic behaviour is further validated by solving the time-dependent heat conduction equation

$$\rho C_p \partial T / \partial t = k \nabla^2 T + Q_{\text{gen}}(t) \quad (12)$$

The thermal response time is expressed as

$$\tau_{\text{thermal}} = \rho C_p V / (h_{\text{eff}} A_{\text{cooling}}) \quad (13)$$

where  $\rho C_p$  is the thermal mass,  $V$  the heated volume, and  $A_{\text{cooling}}$  the cooling surface area. This relationship underscores the importance of minimising the thermal inertia and optimising the heat dissipation pathways to achieve high-speed modulation. As the spatial distribution of the absorbed pump power differs between the 1D and 2D excitation schemes, the effective heated volume  $V$  and cooling boundary area  $A_{\text{cooling}}$  are not the same in the two cases. Consequently, their thermal time constants  $\tau_{\text{thermal}}$  differ, leading to distinct phase delays and transient waveform shapes under dynamic modulation.

The experimental results across the frequency range of 200 Hz to 100 kHz are presented in **Fig. 8a—8d**, where the 1D and 2D modulation traces consistently exhibit different waveform shapes and phase delays, in agreement with the above thermodynamic analysis. At 200 Hz (**Fig. 8a**), the output waveform closely follows the square-wave input, indicating operation within the quasi-static regime ( $\tau_{\text{thermal}} \ll T$ ) and full thermal tracking. The rise times, defined as the time required for the output to

increase from 10% to 90% of the steady-state amplitude, were measured as 356  $\mu\text{s}$  and 340  $\mu\text{s}$  for 1D and 2D modulation, respectively. These values reflect the effective thermal response time of the device in the low-frequency regime. At 30 kHz (**Fig. 8b**), the output began to exhibit a smoothed, sinusoidal-like shape. This transition occurred because thermal cycles cannot fully settle within each modulation period at higher frequencies, leading to thermal inertia-dominated dynamics.

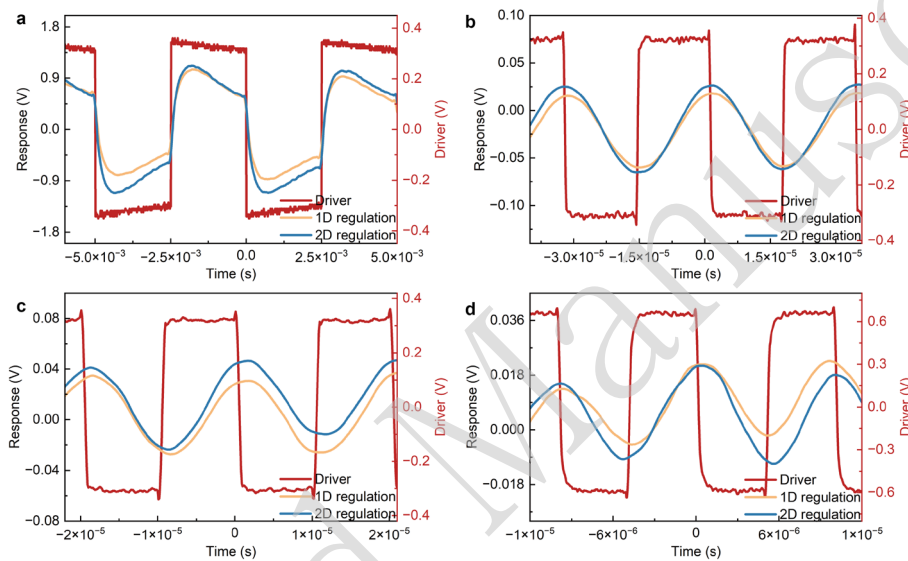


**Fig. 8** Dynamic modulation characteristics of the  $\text{Ag}_2\text{Te}$  QD-coated MRR under different modulation frequencies. A square driving voltage with 8 V amplitude was applied at modulation frequencies of **a** 200 Hz, **b** 30 kHz, **c** 50 kHz, and **d** 100 kHz.

At 50 kHz (**Fig. 8c**) and 100 kHz (**Fig. 8d**), the response became increasingly sinusoidal and exhibited a reduced amplitude, which is consistent with the thermal low-pass filter behaviour described by the dynamic model. The QD-coated MRR demonstrated robust and high-contrast modulation even at 100 kHz, indicating a response limit of 100 kHz—substantially surpassing the typical bandwidth of conventional polymer-based MRRs. This improvement is attributed to the rapid and localised photothermal response enabled by the  $\text{Ag}_2\text{Te}$  QDs, which feature strong absorption and fast non-radiative relaxation.

In addition, the 2D optical control scheme consistently yielded a higher modulation amplitude than that of 1D pumping along the x-axis under identical conditions, particularly at high frequencies. This enhancement is attributed to the expanded excitation volume and improved heat distribution achieved via dual-axis inputs, which enables faster thermal accumulation and reduces the required pump power. For instance, at 100 kHz, x-axis 1D modulation requires 10.68 mW of pump power to maintain the desired modulation amplitude, while the same modulation depth can be achieved under 2D modulation using only 6.20 mW, corresponding to a 42% reduction in power consumption. Notably, because both modulation schemes employ the same optical setup, no additional insertion losses are introduced in the 2D configuration.

The frequency responses for both the 1D and 2D modulation schemes were systematically compared at 100 kHz. The -3 dB bandwidth for 1D modulation at 100 kHz is 9.971 kHz (**Fig. S8a**), while 2D modulation achieves a -3 dB bandwidth of 10.136 kHz (**Fig. S8b**), demonstrating the superior dynamic response and wider frequency range of the 2D scheme. Moreover, a comparison of the normalised modulation amplitude versus frequency in the Supplementary Information (**Fig. S9**) further substantiates the efficiency advantage of 2D modulation, particularly at higher frequencies. This operating regime is particularly relevant for high-speed, energy-constrained photonic systems, where power efficiency at elevated modulation frequencies outweighs the cost of additional optical routing.

To further highlight the advantages of the proposed QD-integrated platform, **Table 1** provides a comparative summary of photothermal modulation devices based on polymer waveguide architectures. Within this material platform, the proposed device exhibits a superior combination of tuning efficiency, extinction ratio, switching time, and power consumption under high-frequency operation, particularly under dual-axis excitation, compared with representative systems employing graphene, gold nanoparticles, and carbon-based nanocomposites.

In the broader landscape of TO modulation technologies, silicon-based electro-thermal TO modulators typically achieve faster response times owing to integrated electrical heating,<sup>42, 43</sup> whereas polymer-based devices inherently exhibit slower dynamics. Against this backdrop, the present work demonstrated a fully all-optical photothermal modulation paradigm that offers complementary advantages beyond response speed. This electrically isolated architecture provides strong immunity against electromagnetic interference and flexible all-optical wavelength control, making it attractive for energy-efficient, high-frequency photonic applications.

**Table 1.** Comparison of photothermal modulation performance in polymer-based waveguide devices.

TO	WS	EG	ST ( $\mu$ s)	PC@HF (mW)	TE (pm/mW)	ER (dB)	Ref.
PDMS+Yb	Polymer-MRR	1D	-	-	15.6	10	44
Graphene	Polymer-MZI	1D	980/520	-	-	13.5	28
EpoCore	Polymer-MZI	1D	400/600	-	-	26.5	45
Carbon nanotube	Polymer-MRR	1D	-	-	30	9.6	29
Au nanoparticles	Polymer-MZI	1D	500.9	-	19100	9.83	27
<b>Ag<sub>2</sub>Te QDs</b>	<b>Polymer-MRR</b>	<b>1D</b>	<b>356</b>	<b>10.68</b>	<b>81.7</b>	<b>11.03</b>	<b>This work</b>
<b>Ag<sub>2</sub>Te QDs</b>	<b>Polymer-MRR</b>	<b>2D</b>	<b>340</b>	<b>6.20</b>	<b>104</b>	<b>11.03</b>	<b>This work</b>

TO: Thermo-optic; WS: Waveguide structure; EG: Excitation geometry; ST: Switching time; PC@HF: Power consumption at high-frequency operation (100 kHz in this work); TE: Tuning efficiency; ER: extinction ratio; MRR: Micro-ring resonator; MZI: Mach-Zehnder interferometer.

### Ag<sub>2</sub>Te QD-enabled passive thermal stabilization in the MRR

To quantitatively evaluate the temperature-dependent TO response consistency and short-term thermal stability within the operational regime of the  $\text{Ag}_2\text{Te}$  QD-coated micro-ring, the temperature-dependent spectral responses of both uncoated and coated MRRs were systematically investigated. Both devices exhibited a consistent resonance blueshift with increasing temperature, which originated from the negative TO coefficient of PETA, which reduces the refractive index and shortens the optical path length as the temperature increases. As shown in **Fig. 9a**, the uncoated PETA-based micro-ring exhibited a pronounced linear blueshift in resonance wavelength as the temperature increased from  $22.6^\circ\text{C}$  to  $25.0^\circ\text{C}$ , with a temperature sensitivity of  $-250 \text{ pm } ^\circ\text{C}^{-1}$  and excellent linear correlation ( $R^2 = 0.990$ , **Fig. 9b**).

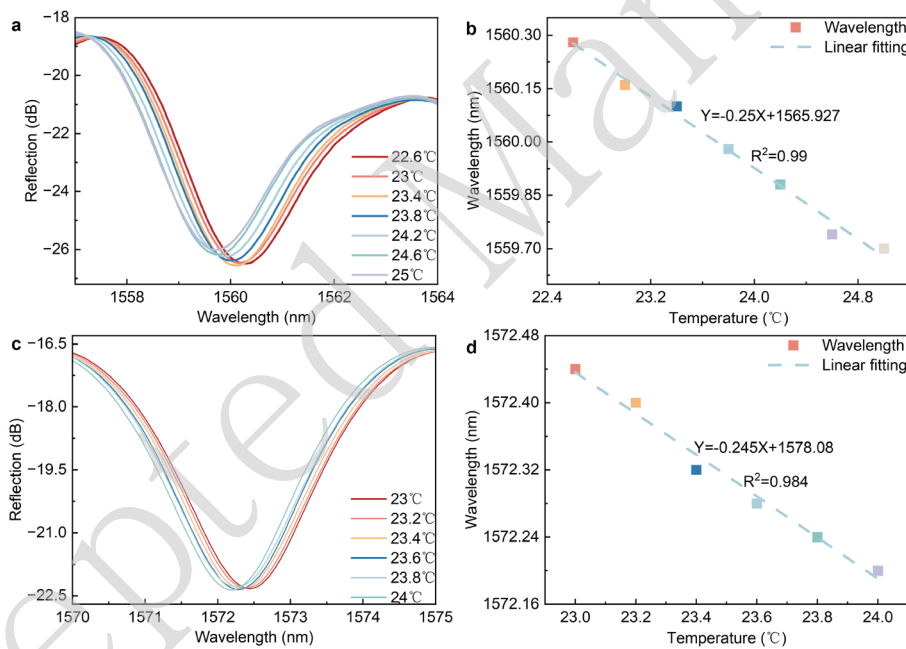


**Fig. 9 a,b** Reflection spectra and linear wavelength shift fitting of the uncoated MRR under thermal variation. **c,d** Corresponding thermal spectral shift and linear dependence for the  $\text{Ag}_2\text{Te}$  QD-coated MRR.

In comparison, the QD-coated device exhibited a highly similar thermal response over a narrower temperature window around room temperature ( $23.0^\circ\text{C}$  to  $24.0^\circ\text{C}$ , in  $0.2^\circ\text{C}$  increments, **Fig. 9c**), yielding a sensitivity of  $-245 \text{ pm } ^\circ\text{C}^{-1}$  with high linearity ( $R^2 = 0.984$ , **Fig. 9d**). Such a temperature window was deliberately selected to ensure

reliable thermal equilibrium and enable a direct comparison between coated and uncoated devices without introducing additional nonlinear thermal effects while remaining substantially below the glass transition temperature of PETA (103°C). This close agreement, despite the additional hybrid layer, demonstrates that the integration of Ag<sub>2</sub>Te QDs does not compromise the intrinsic TO response of the polymeric MRR.

The 6–10 nm spherical Ag<sub>2</sub>Te QDs form discrete nanoscale contact interfaces with the polymer surface rather than a continuous film–substrate contact. According to Hertzian contact mechanics, the contact area between a nanosphere and compliant polymer is confined to the sub-nanometre scale, which significantly limits interfacial shear stress transfer compared with that in conventional thin-film coatings.<sup>46</sup> In addition, the nanoscale dimensions of QDs enable elastic accommodation of thermally-induced deformation at the particle–polymer interface, providing effective mechanical compliance under temperature variation. Such interface-dominated behaviour in polymer–nanoparticle systems has been shown to suppress stress propagation into the host matrix.<sup>47, 48</sup> Consequently, the effective thermal expansion coefficient used in the model is denoted as  $\alpha_{\text{eff}}$  for the uncoated structure and  $\alpha'_{\text{eff}}$  for the coated structure, with  $\alpha'_{\text{eff}} \approx \alpha_{\text{eff}}$  in practice, reflecting the stress-decoupling nature of the nanosphere–polymer interface.

## Conclusion

This study demonstrated a transformative on-chip photonic platform that moves beyond conventional limits, uniquely enabled by two-photon micro-printing. We combined Ag<sub>2</sub>Te QDs with a PETA-based MRR to achieve high-performance 2D all-optical TO modulation. The unparalleled precision of two-photon micro-printing is critical here, allowing for the direct fabrication of intricate hybrid structures on the fibre end, a capability unattainable by traditional planar methods. This advanced manufacturing approach facilitates the strategic integration of Ag<sub>2</sub>Te QDs within the polymer MRR, forming a truly hybrid system that introduces broadband absorption,

interband resonance, and significantly localised field enhancement. Crucially, the 3D fabrication flexibility offered by two-photon micro-printing enables an innovative 2D pumping strategy based on simultaneous optical excitation along both the MRR waveguide (x-axis) and perpendicular to it via the substrate (y-axis). This synergistic approach, combined with the  $\text{Ag}_2\text{Te}$  QD layer's intrinsic LSPR, which amplifies the local optical field intensity by an excellent 300%, synergistically enhances both the static tuning sensitivity and dynamic modulation efficiency. This groundbreaking approach facilitates low-power actuation and fundamentally overcomes the inherent limitations of conventional TO modulation schemes. Experimental results demonstrated a remarkable 19.77-fold increase in tuning efficiency compared with standard polymer MRRs and a dynamic response limit reaching 100 kHz, substantially surpassing the intrinsic speed limits of conventional TO devices, all testaments to the power of this advanced micro-printing-enabled platform.

## Experimental section/Methods

### Synthesis of $\text{Ag}_2\text{Te}$ QDs

$\text{Ag}_2\text{Te}$  QDs were synthesised employing a colloidal solution-phase method. Anhydrous silver acetate (99.5%), tellurium powder (200 mesh, 99.99%), 1-octanethiol (OTT, 98%+), oleylamine (OLA, 90%+), tri-n-butylphosphine (TBP, 98%+), tetrachloroethylene (TCE), and 1-octadecene (ODE, 90%) were used without further purification. A TBP–Te precursor was prepared by dissolving Te powder (0.4 mmol, 51.04 mg) in OLA (4 mL) and TBP (5 mL) under continuous stirring for 3 h. Separately, silver acetate (33.4 mg) was mixed with OTT (1.4 mL) and ODE (10 mL) in a three-neck flask, purged with argon, and heated to 130°C until a clear yellow solution formed. At this temperature, 1.8 mL of the TBP–Te precursor was swiftly injected, and the reaction temperature was immediately reduced to 120°C and maintained for 5 min to allow QD nucleation and growth. The reaction mixture was then cooled, precipitated with acetone (1:5 vol.), and centrifuged at 12000 rpm, and

the purified Ag<sub>2</sub>Te QDs were redispersed in TCE for storage and subsequent use.

### Device Fabrication

Fabrication of Ag<sub>2</sub>Te QDs/PETA/SiO<sub>2</sub> MRR: An MRR structure was fabricated on the end-face of an MMF using PETA (refractive index  $n = 1.48$ ) via a 3D two-photon polymerisation system (MicroLight3D uFAB-3D). The system employs a pulsed laser at 532 nm, with a pulse duration of  $< 0.75$  ns and repetition rate of 10–13 kHz, as specified by the manufacturer. During fabrication, the printing power was set to 12% and scan speed to  $45 \mu\text{m s}^{-1}$ , ensuring high structural fidelity and stable voxel formation. The MRR consists of a straight waveguide, racetrack-shaped micro-ring, and reflective cavity, as shown in **Fig. 2a**. A racetrack-shaped micro-ring was employed to increase the coupling region and enhance the coupling efficiency. The addition of the reflective cavity enables simultaneous input/output from one side, improving the device stability. The straight waveguide has a width of  $d = 3 \mu\text{m}$  and height of  $5 \mu\text{m}$ . The reflective cavity features outer radii of  $R_3 = 10 \mu\text{m}$  and  $R_4 = 12 \mu\text{m}$ . The racetrack-shaped micro-ring features outer and inner radii of  $R_1 = 19 \mu\text{m}$  and  $R_2 = 15 \mu\text{m}$ , respectively, with a coupling length of  $L_c = 6 \mu\text{m}$ . The coupling gap between the straight waveguide and racetrack-shaped micro-ring was precisely controlled at  $0.3 \mu\text{m}$ . To functionalize the MRR with QDs, a wet transfer process was employed. First, Ag<sub>2</sub>Te QDs, stored at low temperature, were uniformly dispersed in a toluene solvent using an ultrasonic cleaner (SKymen JP-020S) for 50 min to eliminate agglomeration. The resulting dispersion was then directly drop-cast and uniformly coated over the entire MRR surface using a micropipette, ensuring conformal coverage across both the micro-ring and waveguide regions. For subsequent optical analysis, the Ag<sub>2</sub>Te QD coating was treated as an effective medium with an effective refractive index of  $n_{\text{eff}} \approx 4.2$ . This process formed an Ag<sub>2</sub>Te QDs/PETA/SiO<sub>2</sub> hybrid structure.

### Characterization

The dimensions of the MRR were evaluated by SEM (Hitachi SU800). Elemental composition analysis was conducted using a Super-X EDS detector integrated into a field-emission scanning electron microscope (FE-SEM). The system offers high spectral resolution with an energy resolution of  $\leq 136$  eV (Mn-K $\alpha$ ), allowing precise identification and spatial mapping of elemental distributions. XRD patterns were recorded using the Cu-K $\alpha$  radiation ( $\lambda = 1.54056$  Å) on an AmartLab XRD system (Rigaku, Japan). The size and morphology of the QDs were characterised by TEM using an FEI Talos F200X G2 instrument operated at an acceleration voltage of 200 kV. The hydrodynamic diameters of the QDs in the colloidal dispersion were determined by DLS using a Malvern particle size analyser. NIR-II fluorescence imaging was performed with a Suzhou NIR-Optics system (China) using an LP1000 filter and exposure time of 200 ms. The UV-VIS-NIR absorption spectra of the QDs were acquired using a HITACHI UH4150 spectrophotometer (Japan). Spectral analysis was conducted using a YOKOGAWA AQ6370D OSA. The 980 nm pump light for excitation was supplied by an FSPSS-974-0300-B. Broadband sources (FSASE-CL-030-B) and a Santec WSL-110 single-wavelength laser were used separately for different measurements. The system was controlled by a Tektronix TDS 2024C oscilloscope for precise dynamic modulation and signal processing.

### Acknowledgements

This research was funded by “Guangdong Basic and Applied Basic Research Foundation(Grant No.2026A1515011145)”, Shenzhen Science and Technology Program (Grant No. SGCX20250526142407010), and Shenzhen Key Industry R&D Program (Grant No. ZDCY20250901095708006)

### Author Contributions

B. D. proposed the original idea and supervised the project. Z.-J. W. fabricated the devices and conducted the main experiments. Z.-J. W. and S.-P. Z. performed optical measurements and processed the experimental data. Y.-L. W. and Z.-H. Y. performed

the numerical simulations and assisted with theoretical analysis. The experimental setup was jointly constructed by B. D. and S.-P. Z. Z.-J. W. drafted the initial version of the manuscript, and B. D. and C.-Y. Y. revised and refined it. All authors discussed the results, contributed to data interpretation, and provided feedback on the final manuscript.

### Data availability

All data are available from the corresponding authors upon reasonable request.

### Conflict of interest

The authors declare no competing interests.

### References

1. Bogaerts, W. et al. Programmable photonic circuits. *Nature* **586**, 207-216 (2020).
2. Dong, M. et al. High-speed programmable photonic circuits in a cryogenically compatible, visible–near-infrared 200 nm CMOS architecture. *Nature Photonics* **16**, 59-65 (2022).
3. Pérez-López, D. et al. Multipurpose self-configuration of programmable photonic circuits. *Nature communications* **11**, 6359 (2020).
4. Torrijos-Morán, L., Pérez-Galacho, D. & Pérez-López, D. Silicon programmable photonic circuits based on periodic bimodal waveguides. *Laser & Photonics Reviews* **18**, 2300505 (2024).
5. Yao, C. H. et al. Integrated reconstructive spectrometer with programmable photonic circuits. *Nature Communications* **14**, 6376 (2023).
6. Krasnokutskaya, I., Tambasco, J. L. J. & Peruzzo, A. Tunable large free spectral range microring resonators in lithium niobate on insulator. *Scientific reports* **9**, 11086 (2019).
7. Zhao, Y. Q. et al. Cavity-enhanced narrowband spectral filters using rare-earth ions doped in thin-film lithium niobate. *npj Nanophotonics* **1**, 22 (2024).
8. Sun, D. H. et al. Microstructure and domain engineering of lithium niobate crystal films for integrated photonic applications. *Light: Science & Applications* **9**, 197 (2020).
9. Lu, L. L. et al. Advances in chip-scale quantum photonic technologies. *Advanced Quantum Technologies* **4**, 2100068 (2021).
10. Hu, J. K. et al. 2D graphene oxide: a versatile thermo-optic material. *Advanced Functional Materials* **34**, 2406799 (2024).
11. Ilie, S. T. et al. Thermo-optic tuning of silicon nitride microring resonators with low loss non-volatile Sb<sub>2</sub>S<sub>3</sub> phase change material. *Scientific Reports* **12**, 17815 (2022).
12. Clementi, M. et al. Thermo-optically induced transparency on a photonic chip. *Light:*

- Science & Applications* **10**, 240 (2021).
13. Cocorullo, G. et al. Thermo-optic effect exploitation in silicon microstructures. *Sensors and Actuators A: Physical* **71**, 19-26 (1998).
  14. Qiu, C. Y. et al. All-optical control of light on a graphene-on-silicon nitride chip using thermo-optic effect. *Scientific Reports* **7**, 17046 (2017).
  15. Yan, H. et al. Wideband-tunable on-chip microwave photonic filter with ultrahigh-Q U-bend-mach-zehnder-interferometer-coupled microring resonators. *Laser & Photonics Reviews* **17**, 2300347 (2023).
  16. Wei, C. C. et al. Programmable multifunctional integrated microwave photonic circuit on thin-film lithium niobate. *Nature communications* **16**, 2281 (2025).
  17. Liu, Y. B. et al. Parallel wavelength-division-multiplexed signal transmission and dispersion compensation enabled by soliton microcombs and microrings. *Nature Communications* **15**, 3645 (2024).
  18. Lim, J. et al. Ultrasensitive mid-infrared optical gas sensor based on germanium-on-insulator photonic circuits with limit-of-detection at sub-ppm level. *ACS Photonics* **11**, 4268-4278 (2024).
  19. Jiang, X. Y. et al. Programmable photonic solver for computationally complex problems. *ACS Photonics* **10**, 4340-4348 (2023).
  20. Mazuryk, J. et al. Fabrication, characterization, and sensor applications of polymer-based whispering gallery mode microresonators. *ACS Sensors* **10**, 5314-5338 (2025).
  21. Maalouf, A. et al. Wide tunable thermo-optical filters with polymer micro-ring resonators. Proceedings of SPIE 3669, Silicon Photonics and Photonic Integrated Circuits Strasbourg, France: SPIE, 2008, 69961S.
  22. Yamagata, S., Yanagase, Y. & Kokubun, Y. Wide-range tunable microring resonator filter by thermo-optic effect in polymer waveguide. *Japanese Journal of Applied Physics* **43**, 5766-5770 (2004).
  23. Xu, X. C. et al. Nanofabrication of polymer micro-ring resonator on a soft substrate as a flexible ultrasonic detector (Conference Presentation). Proceeding of SPIE PC13319, Photons Plus Ultrasound: Imaging and Sensing 2025. San Francisco, CA, USA: SPIE, 2025, PC133190K.
  24. Lv, H. L. et al. Polymer-based microring resonator with the multimode interference coupler operating at very-near-infrared wavelengths. *Applied Sciences* **9**, 2715 (2019).
  25. Morarescu, R. et al. Fabrication and characterization of high-optical-quality-factor hybrid polymer microring resonators operating at very near infrared wavelengths. *IEEE Photonics Journal* **8**, 6600409 (2016).
  26. Liaw, D. J. et al. Advanced polyimide materials: syntheses, physical properties and applications. *Progress in Polymer Science* **37**, 907-974 (2012).
  27. Cui, A. Q. et al. All-optical organic-inorganic hybrid waveguide switches based on photothermal effect of Au-MOF composites. *Advanced Functional Materials* **34**, 2401880 (2024).
  28. Song, Q. Q., Chen, K. X. & Hu, Z. F. Low-power broadband thermo-optic switch with weak polarization dependence using a segmented graphene heater. *Journal of*

- Lightwave Technology* **38**, 1358-1364 (2020).
29. Yang, L. et al. Short carbon nanotube nano-film-based polymer/SiO<sub>2</sub> hybrid waveguide micro-ring filter. *ACS Applied Materials & Interfaces* **15**, 28555-28562 (2023).
  30. Houtepen, A. J. et al. Colloidal quantum dots for optoelectronics. *Nature Reviews Methods Primers* **5**, 42 (2025).
  31. Katsumi, R., Ota, Y. & Benyoucef, M. Telecom-band quantum dots compatible with silicon photonics for photonic quantum applications. *Advanced Quantum Technologies* **8**, 2300423 (2025).
  32. Georgakilas, I. et al. Room-temperature cavity exciton-polariton condensation in perovskite quantum dots. *Nature Communications* **16**, 5228 (2025).
  33. Chen, M. Y. et al. Integration of colloidal quantum dots with photonic structures for optoelectronic and optical devices. *Advanced Science* **8**, 2101560 (2021).
  34. Zhang, C. et al. Plasmon-assisted broadband all-optical control of highly intense femtosecond laser by weak continuous-wave laser. *Advanced Optical Materials* **8**, 2000560 (2020).
  35. Chen, S. H. et al. Biosynthesis of NIR-II Ag<sub>2</sub>Se quantum dots with bacterial catalase for photoacoustic imaging and alleviating-hypoxia photothermal therapy. *Small* **20**, 2310795 (2024).
  36. Carbajal-Valdez, R. et al. Thermo-optic characterization of graphene oxide quantum dot semiconductors for the determination of quantum efficiency. *Journal of Materials Science: Materials in Electronics* **35**, 848 (2024).
  37. Martins, V. M. et al. Determination of the energy transfer efficiency between CdSe/ZnS quantum dots with two different sizes through a photothermal approach. *Journal of Luminescence* **198**, 198-202 (2018).
  38. Lee, E. S. et al. Frequency response of thermo-optic phase modulators based on fluorinated polyimide polymer waveguide. *Polymers* **14**, 2186 (2022).
  39. Zhang, S. P. et al. PETA polymer/graphene composite film-enabled optical microcavity relative humidity sensor for respiratory monitoring. *ACS Applied Electronic Materials* **6**, 7439-7447 (2024).
  40. Farsari, M. & Chichkov, B. N. Two-photon fabrication. *Nature photonics* **3**, 450-452 (2009).
  41. Von Freymann, G. et al. Three-dimensional nanostructures for photonics. *Advanced Functional Materials* **20**, 1038-1052 (2010).
  42. Tang, Z. L. et al. High-efficiency cladding-free thermo-optic modulators via 1T'-MoTe<sub>2</sub>/silicon waveguides. *ACS nano* **19**, 27794-27803 (2025).
  43. Liu, S. P. et al. Thermo-optic phase shifters based on silicon-on-insulator platform: state-of-the-art and a review. *Frontiers of Optoelectronics* **15**, 9 (2022).
  44. Velázquez-Benítez, A. M., Cano-Velázquez, M. S. & Hernández-Cordero, J. Fiber coupled optically tunable polymer/glass microring resonators. Latin America Optics and Photonics Conference. Medellin Colombia: Optica Publishing Group, 2016, LTu5C. 5.
  45. Niu, D. H. et al. 850-nm polymeric waveguide thermo-optic switch with low power-consumption. *Optics & Laser Technology* **132**, 106476 (2020).

- 
46. Fischer-Cripps, A. C. The Hertzian contact surface. *Journal of materials science* **34**, 129-137 (1999).
  47. Guo, D., Xie, G. X. & Luo, J. B. Mechanical properties of nanoparticles: basics and applications. *Journal of physics D: applied physics* **47**, 013001 (2014).
  48. Bansal, A. et al. Controlling the thermomechanical properties of polymer nanocomposites by tailoring the polymer–particle interface. *Journal of Polymer Science Part B: Polymer Physics* **44**, 2944-2950 (2006).